Research Article | Vol. 14, No. 9 / 1 Sep 2023 / Biomedical Optics Express 4845
Biomedical Optics EXPRESS

Comparative analysis of full-field OCT and optical transmission tomography

SAMER ALHADDAD,[1] OLIVIER THOUVENIN,[1] MARTINE BOCCARA,[2] CLAUDE BOCCARA,[1] AND VIACHESLAV MAZLIN[1,*]

[1] *Institut Langevin, ESPCI Paris, PSL University, CNRS, 1 rue Jussieu, 75005 Paris, France*
[2] *Institut de Systématique, Evolution, Biodiversité (ISYEB), Muséum National d'Histoire Naturelle, Sorbonne Université, EPHE, UA, CNRS ; CP 50, 57 rue Cuvier, 75005 Paris, France*
[*] *mazlin.slava@gmail.com*

Abstract: This work compares two tomographic imaging technologies, time-domain full-field optical coherence tomography (FFOCT) working in reflection and optical transmission tomography (OTT), using a new optical setup that combines both. We show that, due to forward-scattering properties, the axial sectioning and contrast in OTT can be optimized by tuning illumination. The influence of sample scattering and thickness are discussed. We illustrate the comparison of the two methods in static (morphology) and dynamic (metabolic contrast) regimes using cell cultures, tissues and entire organisms emphasizing the advantages of both approaches.

1. Introduction

Transmission bright field imaging is indispensable for observing morphology of biological samples. At the origin of image formation is the phenomenon of light interference between the transmitted and scattered waves [1,2]. The classical work of Zernike [3] demonstrated the ability to control image contrast by varying the relative phase between the waves. Further advancements allowed to perform quantitative phase measurements [4]. These techniques excel at imaging semitransparent biological samples. However, analyzing thick and scattering samples is challenging since the in-focus structures of interest can be hindered by the light coming from out-of-focus sample layers. This can decrease the image quality and result in a loss of information, making it difficult to analyze the sample accurately.

Another class of approaches that are commonly used for imaging thick samples are based on interferometry of backscattered light. Optical coherence tomography (OCT) is one such technique that relies on broadband illumination spectrum, an interferometer, and a spectrometer to reconstruct tomographic views of the sample without out-of-focus light [5,6]. A specific subtype of OCT, known as time-domain full-field OCT (FFOCT) takes advantage of 2D cameras to obtain en face images [7,8]. The tomographic images are then reconstructed from a sequence of camera frames, each containing a distinct light interference pattern or optical phase. FFOCT has been applied to various imaging problems, such as cancer biopsy analysis [9], visualization of organoid development [10], fingerprint identification [11], and ophthalmology [12–15].

Recently, we introduced a transmission-based optical sectioning approach, called optical transmission tomography (OTT) [16]. Similar to FFOCT, OTT reconstructs tomographic images from a sequence of phase-shifted camera frames. Compared to OCT methods, OTT has its axial resolution, determined by the numerical aperture. In addition to the static tomographic views, the above phase-based methods can produce color-coded images of intrinsic metabolic cell dynamics.

The aim of this paper is to provide a comparative analysis of FFOCT and OTT and to illustrate the differences between these two approaches using a few model cases. To achieve this goal, we combined FFOCT and OTT in a single microscope to image the same field of view with both modalities. We first briefly describe the principles of both techniques and then demonstrate that,

#494585 https://doi.org/10.1364/BOE.494585
Journal © 2023 Received 2 May 2023; revised 25 Jul 2023; accepted 26 Jul 2023; published 24 Aug 2023

Biomedical Optics EXPRESS

due to forward scattering properties, axial resolution in OTT depends on the illumination and is object dependent. Taking advantage of this effect, we propose adding a diffusive layer between the illumination and the object in OTT. We discuss a newly discovered compromise between sectioning and contrast that is specific to OTT, as well as the influence of thickness of samples observable with this modality. Finally, we use FFOCT-OTT microscope to compare tomographic images of both modalities acquired in transparent zebrafish embryos and different murine organs, showing that the accessible contrast can be significantly different.

2. Methods

2.1. Combined FFOCT-OTT system

FFOCT is composed of a Linnik interferometer with identical microscope objectives (MO) (water-immersion 40X Nikon CFI APO, 0.80 numerical aperture (NA), 3.5 mm working distance (WD)) in the sample and reference interferometric arms. Illumination is provided by an incoherent $\lambda = 660$ nm light-emitting diode (LED) (M660L3, Thorlabs, USA) to avoid light speckle and cross-talk artifacts. The LED has low temporal coherence with a spectral bandwidth of 25 nm, which determines axial resolution, similar to conventional OCT. The reference arm is equipped with a mirror (silicon wafer, 40% reflectivity at 660 nm) mounted on a piezoelectric motorized stage (STr-25/150/6, Piezomechanik GmbH, Germany). The piezo stage modulates the mirror position in time, controlling the optical phase delay (0 or π) between the sample and reference light beams. The camera (Q-2A750-CXP, Adimec, Netherlands) sequentially captures two phase-shifted frames. Subtracting one frame from another rejects the non-interfering light from the rest of the sample and produces an en face tomographic view of the slice of interest.

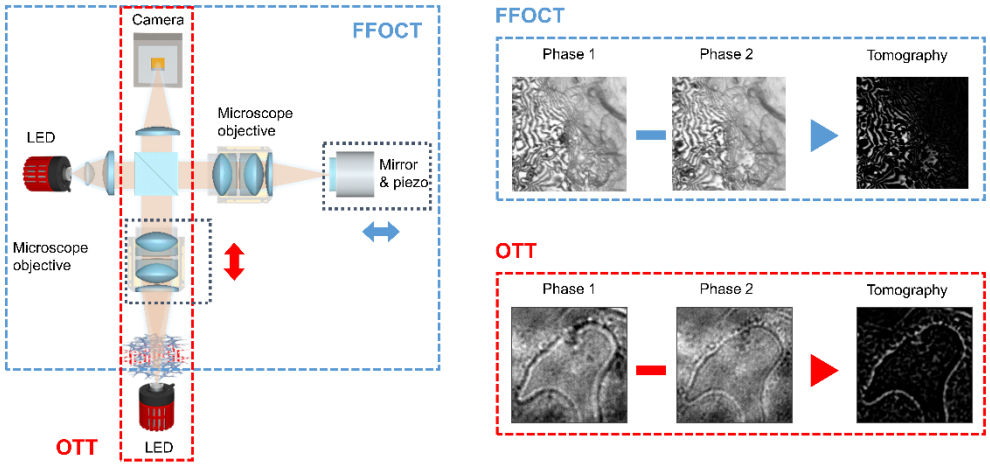

Fig. 1. Combined FFOCT-OTT setup and principles of tomographic reconstruction.

OTT is integrated into FFOCT through an additional LED (M660L3, Thorlabs, USA) located underneath the sample (Fig. 1). OTT relies on a common-path transmission interferometer geometry, described in detail in [16], where light scattered by the sample interferes with light transmitted through the sample. Although the two beams propagate along the same optical path, they differ in divergences, with the scattered wave filling a larger portion of the objective's numerical aperture. One can control the phase delay between the two beams using the Gouy effect - a π optical phase shift that a light wave exhibits when passing through the optical focus. Gouy phase shift appears as a fundamental property of the focused Gaussian beam model [17]. By axially moving the objective lens, we change the optical phase of the light beam scattered

Biomedical Optics EXPRESS

from the in-focus slice of the sample. Similar to FFOCT, sequentially acquired phase-shifted frames can be subtracted from one another to reject the out-of-focus light that is not affected by the Gouy phase shift and reconstruct the en face tomographic view.

FFOCT and OTT acquisitions are not simultaneous; when one LED is working, the other is disabled.

2.2. Biological samples under study

Zebrafish larvae are a reliable model organism due to their transparency, small size, fast development, genetic tractability and similarity to human biology. Experiments on larvae were performed at 5 days post fertilization (dpf) following procedures approved by the Institutional Ethics Committee Darwin in the Institut du Cerveau (ICM). Larvae grew in an incubator at 28.5°C until 5 dpf. Shortly before the experiment, the larvae were laterally mounted in 1.5% low melting point agarose and paralyzed by injecting 0.5 nl of 0.5 mM α-bungarotoxin in the ventral axial musculature. The experiments were performed at room temperature in a physiological solution.

Murine organs were obtained from the partner research institution Institut de la Vision (Paris) as recuperated waste tissue from the unrelated experiment. Imaging was performed within few hours after dissection.

3. Experimental results

The comparison results for the current FFOCT and OTT devices are summarized in Table 1. Each parameter was experimentally verified. While OCT is known for decoupling the axial resolution (dependent on the spectral bandwidth of the light source) from the lateral resolution (dependent on the NA of the imaging optics), this property is not applicable to OTT, where both resolutions depend on NA. Moreover, due to the transmission nature of OTT the resolution depends on a more complex effective NA that encompasses: (1) collection NA_c of imaging optics, (2) illumination NA_i, (3) thickness and scattering properties of the sample below the image plane, which can effectively increase NA_i, (4) $NA_{scatter}$ produced by the local forward scatterer in image plane ($NA_{scatter}$ being determined, for example, by Mie scattering for organelles with the sizes comparable or larger than the wavelength). The mechanisms are illustrated in Fig. 2. In the next sub-sections we will attempt to decouple each of these mechanisms and show, how they affect the Gouy phase. We will then follow up by comparing FFOCT/OTT in terms of signal-to-noise ratio (SNR), dynamic range, exposure time, speckle/fringe artifacts.

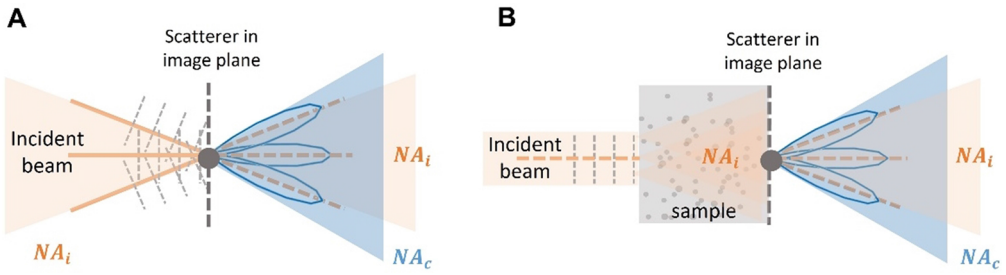

Fig. 2. Mechanisms that control the collection NA_c and resolution in OTT: (A) Illumination NA_i and $NA_{scatter}$, the latter being determined by the scatterer size and Mie theory, (B) Scattering inside the sample further expands the illumination NA_i as well as the $NA_{scatter}$, the latter being determined by the scatterer size and Mie theory.

Biomedical Optics EXPRESS

Table 1. Comparative table of FFOCT and OTT devices

	FFOCT		OTT	
Illumination wavelength	660 ± 12 nm		660 ± 12 nm	
Field of view	260 µm × 260 µm		260 µm × 260 µm	
Type of contrast	Back-scattered (reflection)		Forward-scattered (transmission)	
Tomographic reconstruction	Phase-shifting by modulation of reference mirror		Phase-shifting by modulation of microscope objective (Gouy effect)	
NA_i	0.8		0.8	For illumination geometry that fills NA of microscope objective AND/OR For thick/scattering sample, that creates secondary illumination with high-NA
			0.1 – 0.8	For illumination geometry that underfills NA of microscope objective AND For thin/semi-transparent sample, that does not create secondary illumination
NA_c	0.8		0.1 – 0.8	NA_c = max (0.8, NA_i + $NA_{scatter}$), where: $NA_{scatter}$ is large for small (sub-micron) local organelles that scatter isotropically $NA_{scatter}$ is small for large (> micron) forward scattering organelles
Lateral resolution	0.4 µm	$\frac{\lambda}{2 \cdot NA_c}$	0.4 µm – 3 µm	$\frac{\lambda}{2 \cdot NA_{eff}}$
Axial resolution	6 µm	$\frac{1.4 \cdot \lambda^2}{\pi \cdot n \cdot \Delta\lambda}$	0.6 µm – 60 µm	$\frac{2 \cdot \lambda \cdot \left(n^2 - NA_{eff}^2\right)}{\pi \cdot n \cdot NA_{eff}}$
SNR (one image)	35 dB		45 dB	
Dynamic range	5% signal in 16-bit background (for 40% reflectivity mirror)		50% signal in 16-bit background (standard LED illumination in weakly scattering sample)	
Exposure time	20 ms		20 ms – 300 ms	Exposure time is longer for scattering/thick samples
Speckle/Fringe artifacts	- Highly correlated fringe patterns, due to interference with a single flat mirror - High frequencies of fringes: 300 nm axial variation in the sample produces π phase shift		- Low correlation of fringe patterns, due to self-interference of random scatterers - 10× lower frequency of fringes comparing to FFOCT for the same axial resolution. For example, for 6 µm axial resolution, π shift of fringe's phase (dark to bright) is produced by 6 µm axial variation within the sample	

*NA_i and NA_c are the numerical apertures of illumination and collection, respectively. NA_{eff} = (NA_i + NA_c)/2 is the effective numerical aperture of the system. Refractive index of the sample is assumed to be 1.4.

Biomedical Optics EXPRESS

3.1. Axial resolution in OTT under variable illumination

To investigate the effect of illumination on the axial resolution in OTT, we performed three tests: (1) standard illumination with LED; (2) low-NA_i illumination produced by covering LED with an aperture; (3) high-NA_i illumination produced by placing a scattering medium (16 parafilm layers about 2 mm in total thickness) between the LED and the sample, which extended the effective light source. In all the tests the LED was located at 1 cm from the image plane, and we used the zebrafish tail as a sample.

For simplicity we began by comparing the direct transmission microscopy images without phase modulation (Fig. 3(A) and Visualization 1). We found that extending the light source and, thus the illumination NA_i, using the parafilm decreased the depth-of-field (separate zebrafish layers are distinguishable), while the apertured small NA_i illumination resulted in depth-of-field increase (overlap of zebrafish layers from all the depths). This illustrates that the effective detection NA is determined by both the imaging optics NA and illumination NA_i - a result well-known in conventional transmission microscopy. The interesting effect is that Gouy optical phase shift (interferometric contrast inversion around the focus) exhibits similar behavior – the axial phase shift profile extends with the increasing depth-of-field (Fig. 3(B)). This means that resolution in tomographic OTT images, formed by the subtraction of the two Gouy phases (dark-to-bright, the π-phase-shifted), can be controlled by the combination of the illumination NA_i and NA of imaging optics (Fig. 3(C)). Using high-NA_i illumination we were able to efficiently suppress the out-of-focus zebrafish layers (Fig. 3(D)) and improve the contrast. If desired, a different contrast, resembling typical tomographic contrasts, can be obtained by removing the negative values in the image via adjusting the brightness/contrast in the histogram.

Curiously, we observed that the improvement in axial resolution in OTT comes at a cost of the decrease in Gouy phase contrast (Figs. 3,4). Indeed, the gradual increase in parafilm thickness steadily decreases the effective dynamic range of the signal within the total 16-bit range. For example, the signal without the parafilm varies between 30,000 - 65,536 equivalent to 50% of the 16-bit range (the remaining being the background light), while the signal with the 16-layer parafilm varies between 50,000–65,536 equivalent to only 20% (Fig. 4(A)). By measuring the relations between 1) the parafilm thickness and axial resolution (similarly to Fig. 3) and 2) the parafilm thickness and standard deviation of the signal variations (representative of contrast), one can find that the contrast has an inverse linear relationship with the resolution. In order to explain it, we used a separate OTT system equipped with a microscope objective (PA100X-INF-IRIS, Amscope) that had an accessible back-focal plane, and imaged fibers of the optical cleaning tissue (Fig. 4(B)). Our findings showed that the interference contrast in the image plane completely vanishes, when the illumination NA_i fills the detection NA. This case is hypothesized to be caused by the transmitted and scattered beams having similar angular divergences and similar phases, as a result no interference phenomena can be observed. We also acknowledge that changing the illumination size also affects spatial coherence, which may also account for the observed loss of contrast. In the intermediate cases, the more collimated is the illumination beam, the larger is the overall angular separation between the transmitted and scattered beams, leading to a larger interference contrast in the image. In general, we estimate that an illumination NA of about 10 to 20% lower than the objective NA should ensure both spatial coherence, interference contrast, and resolution.

It is important to note the similarities between imaging with the scattering layer and imaging thick samples. Indeed, the sample thickness below the image plane acts as a scattering parafilm between the light source and the sample. The thicker is the sample the broader is the secondary illumination of the imagine plane and the more filled is the numerical aperture, leading to reduction of interferometric contrast. The best resolution-contrast tradeoff depends on the sample thickness and the degree of scattering.

Biomedical Optics EXPRESS

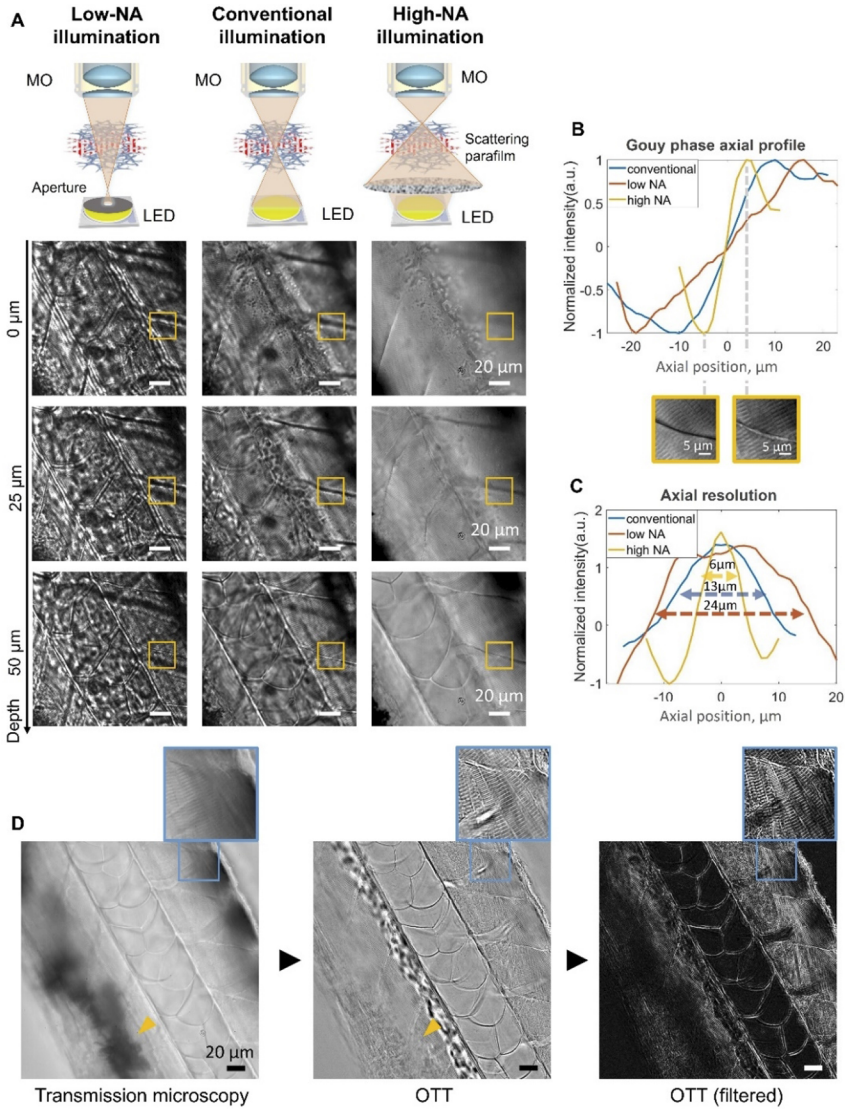

Fig. 3. Three configurations of illumination in OTT (low-NA_i, standard and high-NA_i source) and their effects on the axial sectioning and contrast in live zebrafish larva. Aperture and scattering parafilm were placed between the LED and sample for low-NA_i and high-NA_i illuminations respectively. For simplicity, (A) shows transmission microscopy images acquired without phase modulation. Through-depth sequences are available in Visualization 1. Gouy phase axial profile extends together with the depth-of-field following the decrease of the illumination NA_i (B). These axial profiles were measured from the linear structure in the yellow square in (A). Resolution curves (C) were computed as a difference between the π-phase-shifted (dark-to-bright) axial intensity curves in (B). The axial resolutions, measured at full-width-half-maximum (FWHM), ranged from 6 µm (high-NA illumination) to 24 µm (low-NA illumination) for this particular linear structure, but would have been different for structures of different sizes, as is discussed in the next sub-section below. Improvement in sectioning with high-NA comes at a cost of decreasing the Gouy phase contrast. Comparing to transmission microscopy, OTT improves the contrast and rejects the out-of-focus structures, pointed by the yellow arrows in (D). OTT-filtered view is obtained by removing the negative values in the image via tophat filter or by adjusting the brightness/contrast in the histogram.

Biomedical Optics EXPRESS

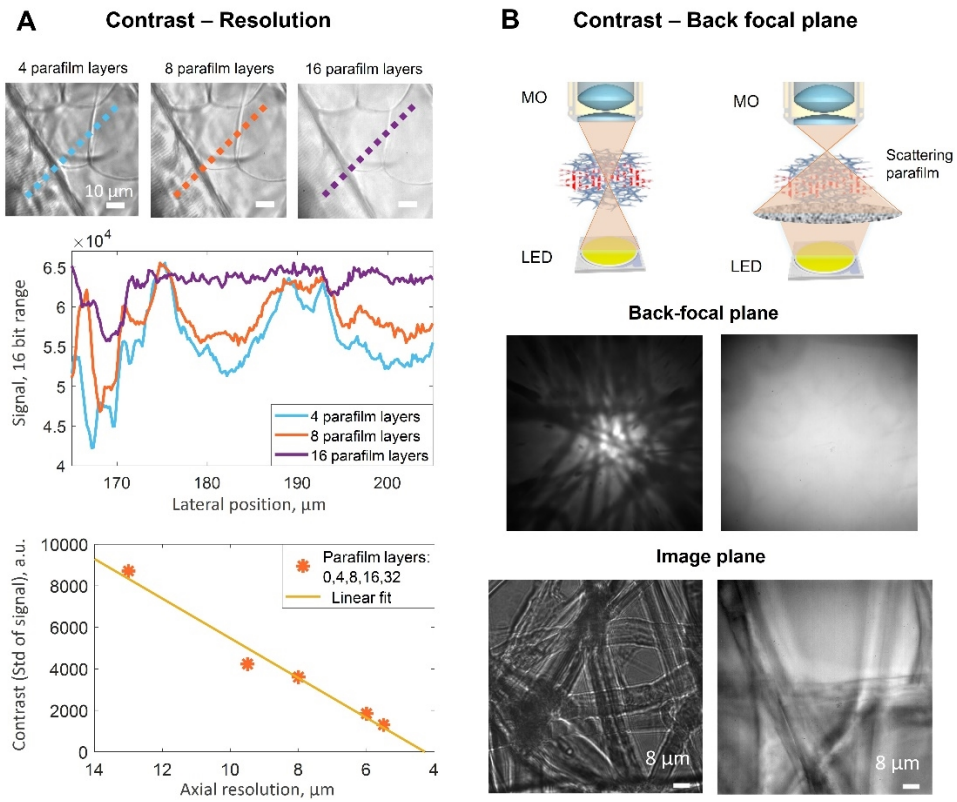

Fig. 4. Relation of Gouy phase contrast with resolution in OTT. Different number (0, 4, 8, 16, 32) of parafilm layers were put between the LED and the zebrafish sample. The thicker was the parafilm the smaller proportion of the total dynamic range was left for the signal (most dynamic range was taken by the background). Contrast, measured as standard deviation of the signal profiles, showed inverse linear relation to the resolution (A). The Gouy contrast completely disappears, when parafilm becomes sufficiently thick to scatter light within the full objectve's numerical aperture (B). This is hypothesized to correspond to the case, of the transmitted and scattered waves becoming co-aligned and exhibiting the same phase. In (B) the optical cleaning tissue was used as a sample.

3.2. *Axial resolution in OTT for various scatterer sizes*

Finally, we would like to illustrate that the axial resolution in OTT is locally dependent on the nature of the scattering objects (Fig. 5).

The angular distribution of the forward scattering can vary drastically depending on the particle size. For instance, for SiO_2 particles of 60 nm, 600 nm and 6000 nm diameter illuminated by a 660 nm plane wave the angular scattering distribution is given by the anisotropic scattering parameters $g = 0.025$, 0.87 and 0.95 respectively (Fig. 5(A)) [18]. Here we considered the Mie scattering regime, where the large particles (size close or larger than the wavelength) are predominantly scattering forward in the same direction as incident light. This means that particles of varying sizes can fill different portions of the detection NA and, therefore, visibly exhibit different depth-of-field.

Similar principle is seen in the zebrafish sample (Fig. 5(B)). Biological structures are predominantly forward scatterers [19], nevertheless the degree of angular divergence can differ from one structure to another. Small structures exhibit the fast Gouy phase shift across the optical

Biomedical Optics EXPRESS

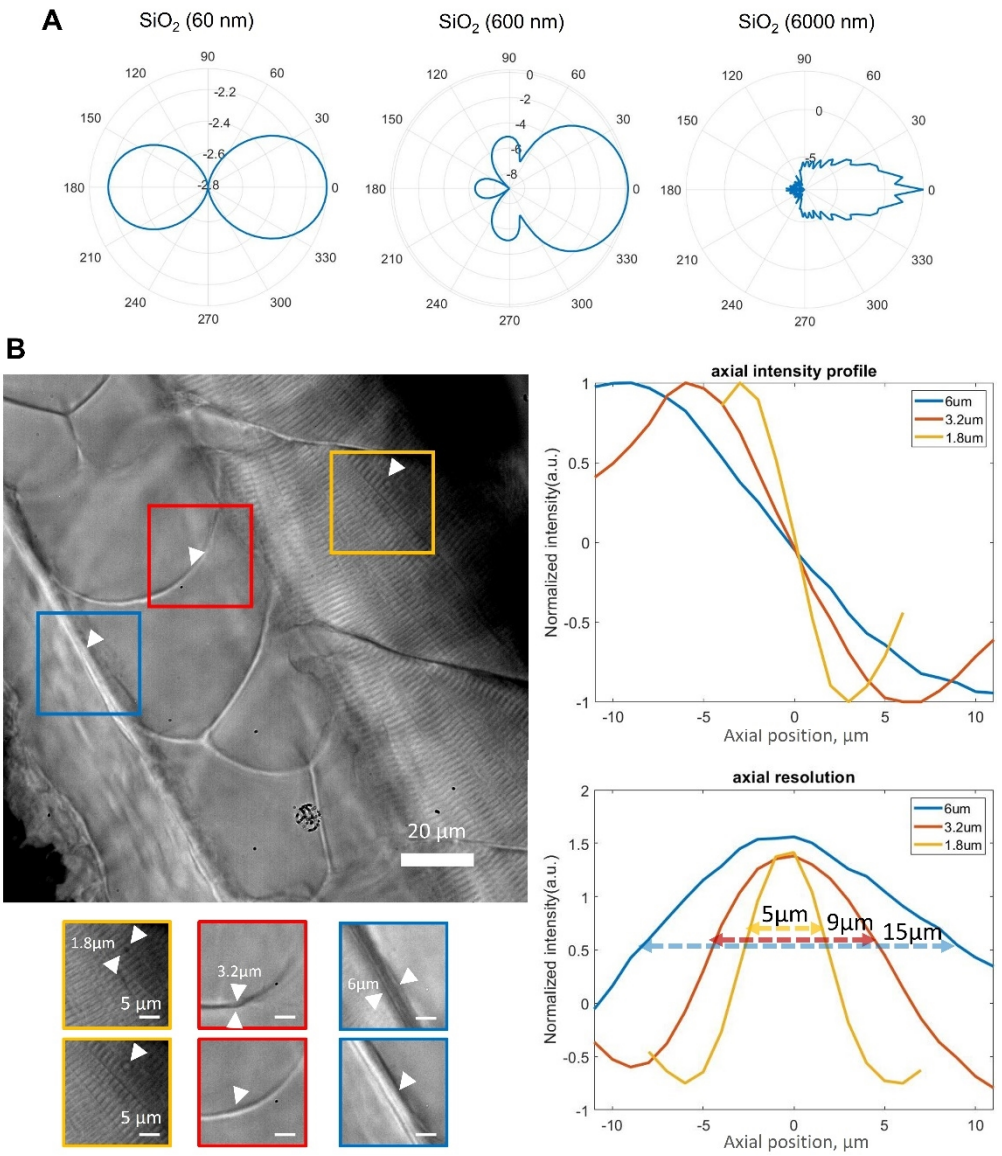

Fig. 5. Resolution in OTT depending on the size of the scatterer. (A), Mie scattering intensity from SiO_2 particles (n = 1.45) of different sizes in water (n = 1.33) presented in logarithmic scale. (B), Gouy phase profiles and resolution curves for scatterers of different sizes in zebrafish. The experiment used high-NA illumination with parafilm layer. Resolution curves were computed as a difference between the π-phase-shifted (dark-to-bright) axial intensity curves. Small particles produce broader angular scattering and fill larger portion of the NA, which leads to their shallower visible depth-of-field and higher resolution.

focus (~ 5 µm), as the divergently scattered light wave fills the larger portion of the detection NA. On the other hand, the larger structures that scatter light in the forward direction, underfill the NA and are effectively seen with larger depth of field (~ 20 µm).

Biomedical Optics EXPRESS

Overall the detection NA and the effective resolution depend on the combination of the illumination NA, thickness/scattering of the sample and, locally, on the angular distribution of the scattering from the individual scatterers.

3.3. Tomographic FFOCT/OTT image comparison

Below we provide comparison of tomographic FFOCT and OTT images obtained by subtraction of the two phase-shifted camera frames. During the OTT acquisition the scattering parafilm was placed between the LED and the sample to improve the axial resolution. Figures 6 and 7 present results from the zebrafish larvae tail and mouse organs (brain, peritoneum, heart), respectively.

FFOCT demonstrates higher optical sectioning and better rejection of the out-of-focus light than OTT. This is expected, given that OTT is known to: 1) have finite damping of the out-of-focus light due to the wings in axial PSF and due to the lateral PSF enlargement with defocus [16], 2) local dependency of axial PSF on the sizes of the scatterers. Despite these factors, OTT produced en face images comparable to FFOCT and we also could reconstruct the cross-sectional (B-scan) and volumetric views (Visualization 2). The latter were useful for resolving the somites, spinal cord and blood vessel in the larvae. There are several other advantages to OTT:

(1) Higher SNR of 45 dB compared to 35 dB in FFOCT, when evaluating the single non-averaged images in both modalities. These numbers are provided as an example and can significantly differ from sample to sample. SNR was measured as $SNR = 10 \cdot \log_{10}(S/\sigma)^2$, where S is the signal from uniformly reflective/transmissive structure of the sample and σ is standard deviation of the noise in the corner of the image outside of the sample. That SNR advantage is caused, on one hand, by the smaller scattering volume of the finer section in FFOCT, and, on another hand, the higher forward scattering of biological tissues benefiting OTT, as well as the higher effective dynamic range for OTT. Indeed, due to the presence of the second optical arm with the highly reflective 40% mirror, the variation of interference signal in FFOCT takes only 5% of the full 16-bit dynamic range of the direct camera frame with the rest being filled by the incoherent background light. On the contrary, in common-path path OTT the signal from the sample accounts for 20% of the full 16-bit camera range (for 16-layer parafilm illumination and even more (50%) for conventional one). It should be noted that some configurations of FFOCT, for example [12], fill larger portion of the dynamic range, by using a reference mirror with a low 4% reflectivity that matches to the reflectivity of the sample.

(2) Lower sectioning of OTT can occasionally make the image analysis easier because the entire sample structures are visible in one field-of-view (FOV). In FFOCT this is not always the case, for example, each FOV shows only parts of length of somites (Figs. 6(A),6(B)).

(3) OTT is less affected by the residual interference fringe artifacts that may prohibit resolving the fine cellular mosaics at the resolution limit (Figs. 6(C),6(D)). Comparison of speckle/interference fringe artifacts is detailed in the sub-section below.

Murine tissues can be more complex to image in transmission than transparent zebrafish embryos because of the larger scattering and thickness. Tissue volume underneath the image plane can act as a scattering layer similar to parafilm in the experiment above, which increases the effective illumination NA_i while also diminishing the contrast. In order to reduce this effect, we cut thin the sample layers and flattened them by squeezing between the lower coverslip and a thin optically transparent pellicle membrane. Having this approach in place, we still frequently need to increase the exposure time in OTT to 20 ms – 300 ms (for efficient camera saturation) compared to the unchanged 20 ms in reflection-based FFOCT. Both FFOCT and OTT resolved fine structures across the large depths (see Visualization 3 and Visualization 4), but revealed different contrasts. Particularly, in the brain the axons of cortical neurons were highlighted in

Biomedical Optics EXPRESS

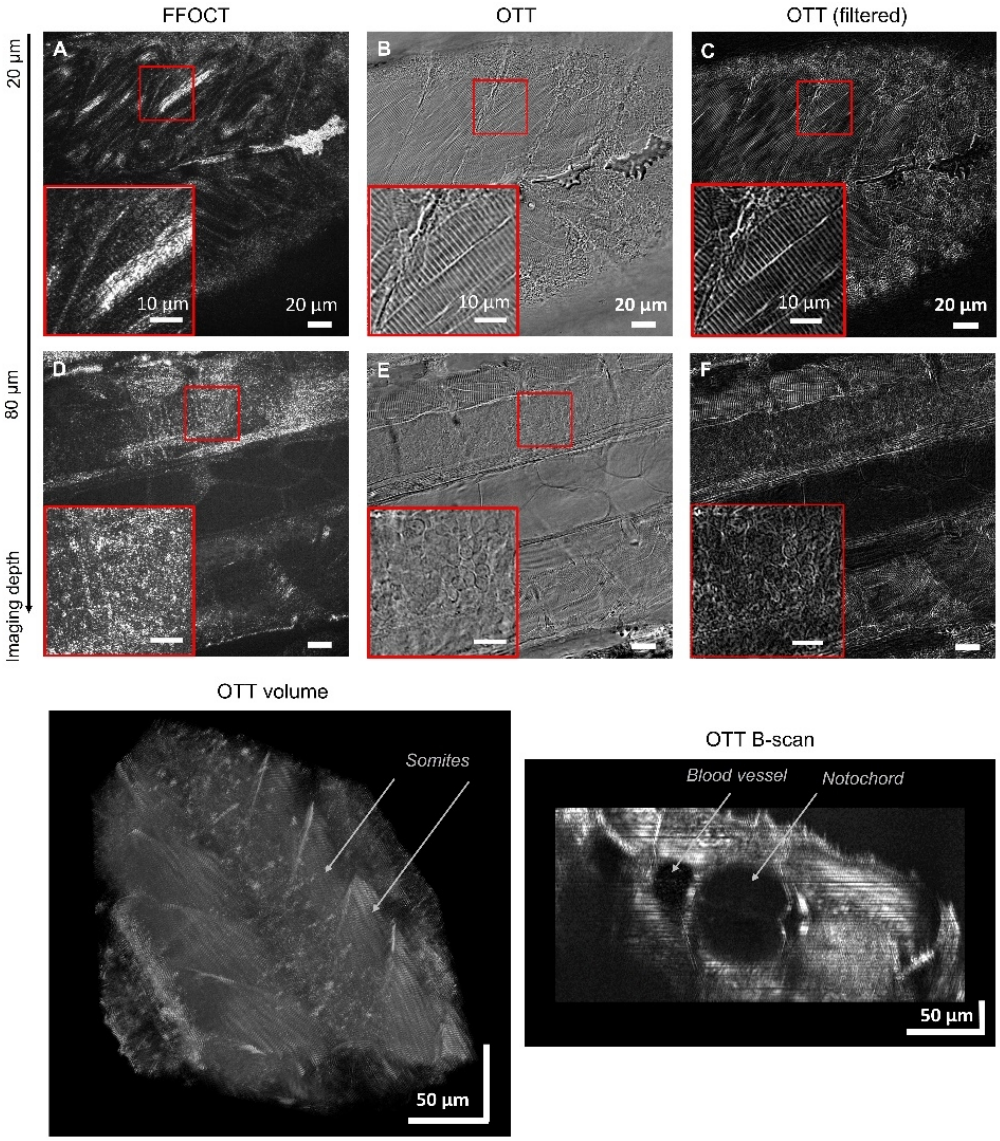

Fig. 6. Tomographic FFOCT (40 averages) and OTT (no averaging) images of live zebrafish larvae tail. Two-phase modulation scheme was used for reconstruction. C, F filtered images of OTT were additionally processed by adjusting the brightness/contrast in the histogram (or by top hat filtering) to reject the negative values following the image subtraction. FFOCT provided finer optical sectioning, while OTT had higher SNR, had more intuitive view of the entire sample structures across the FOV and was less affected by the interference artifacts enabling visualization of the cell mosaics. The rotating volumetric OTT view is provided in Visualization 2. Both FFOCT and OTT were able to successfully resolve different zebrafish structures including notochord, blood vessels, skin layer, cells from spinal cord and some of their axons.

FFOCT, while the neuron cell bodies appeared as dark disks in agreement with reports literature [20,21]. On the contrary, the axons in OTT lacked contrast, but other cell structures were readily detectable.

Biomedical Optics EXPRESS

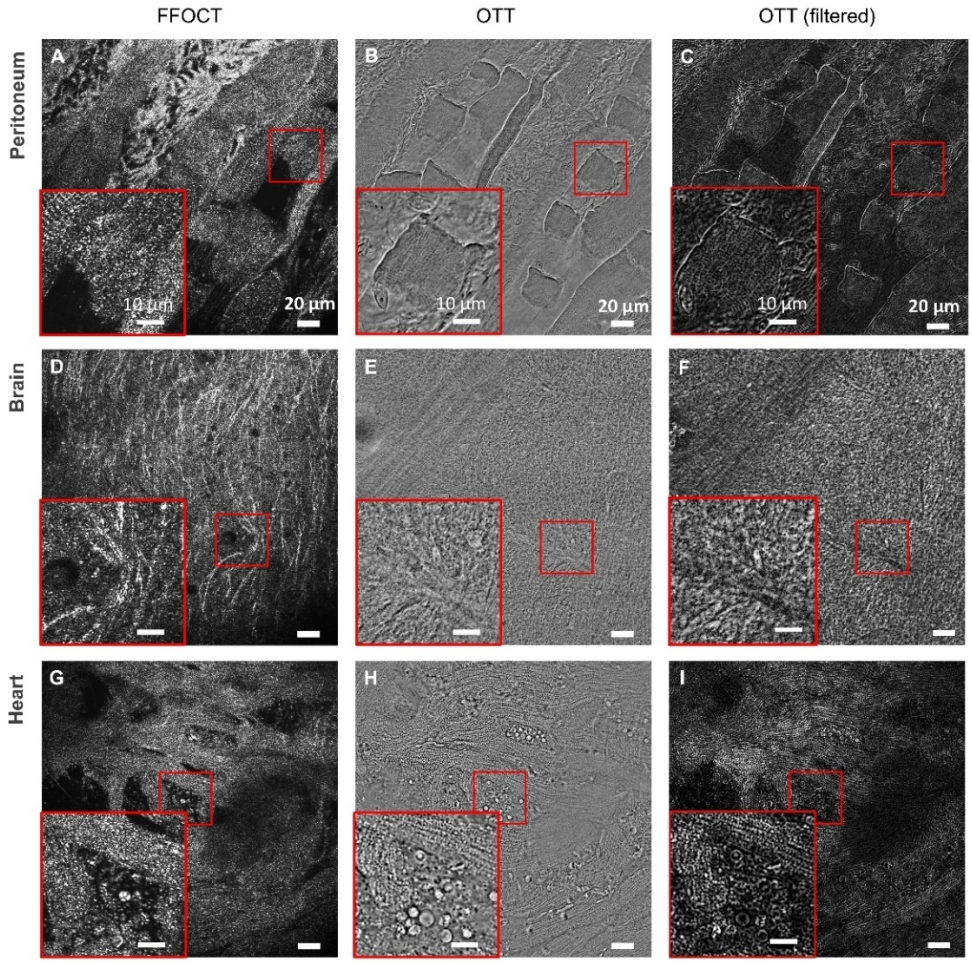

Fig. 7. Tomographic FFOCT (40 averages) and OTT (no averaging) images of mouse organs. Two-phase modulation scheme was used for reconstruction. (C), (F), (I) are filtered images of OTT that were obtained by adjusting the brightness/contrast in the histogram (or, equivalently, by top hat filtering) to reject the negative values following the 2-phase image subtraction. FOV in FFOCT images (A) and (D) are shifted by a few hundred microns comparing to their OTT counterparts. All the samples were imaged at 30 µm depth. Through-depth sequences for brain and heart are available as Visualization 3 and Visualization 4 presents blinking due to faulty LED behavior following the water leakage. Both FFOCT and OTT resolved cell-scale structures, however with a different contrast.

3.4. Dynamic image comparison

Beyond structural contrast, FFOCT and OTT also gained recognition for extracting metabolic information through the analysis of signal fluctuations in time. In particular, FFOCT showed ability to quantify blood flow at cellular detail and at µm/s speed across the entire FOV in live human eye [15,22], while the so called Dynamic FFOCT followed interferometric phase fluctuations connected with the movements of intracellular organelles during the development of organoids [10,23]. Dynamic OTT has also been demonstrated, obtaining metabolic activity of cultured cells and of corneal/retinal cells in explants [16]. However, as FFOCT and OTT do not necessarily capture the same scatterers in their respective backward/forward scattering

Biomedical Optics EXPRESS

configurations, the signal fluctuations due to the scatterers motion might also be different. In this section, we aim to provide comparison of dynamic images in FFOCT versus OTT, first by imaging the blood flow in a zebrafish larva (Fig. 8) and second by imaging the cell dynamics in explant mouse liver (Fig. 9).

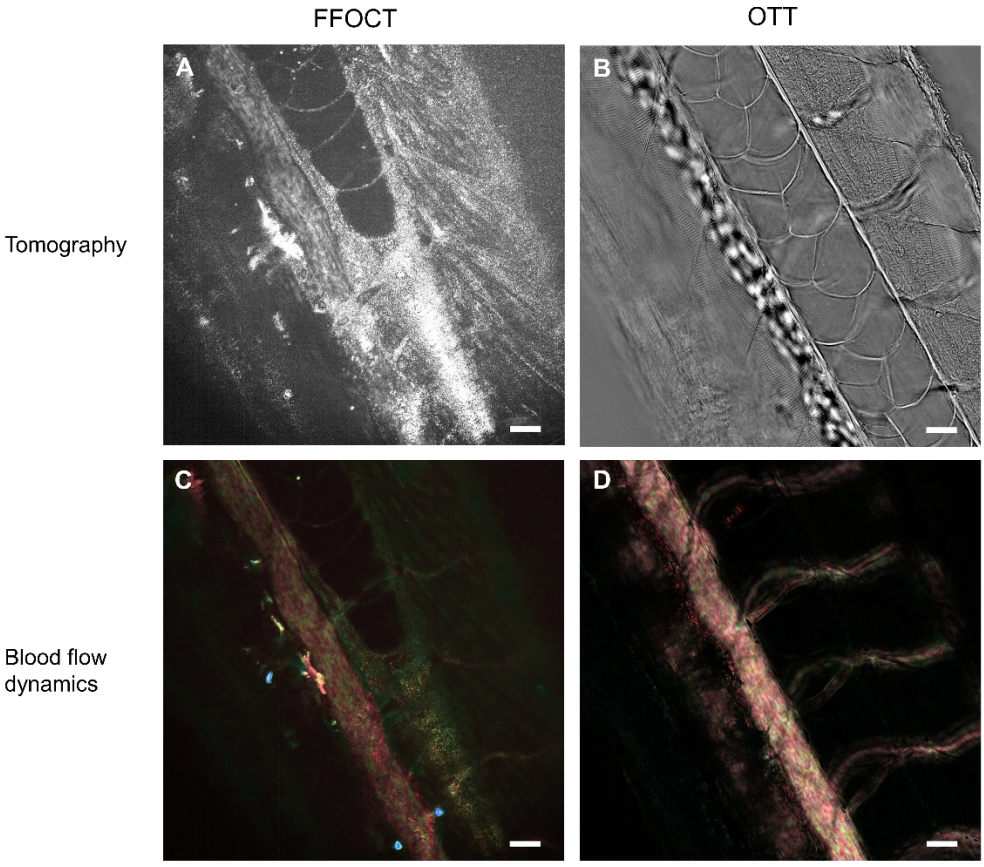

Fig. 8. Blood flow dynamics in FFOCT and OTT in zebrafish embryo. OTT shows more vessels due shallower depth-of-field. Scale bars are 20 µm.

Following the blood flow, the erythrocytes change their location in sequentially captured camera fames. A known result is that in the reconstructed (via image subtraction) FFOCT/OTT tomographic images we can always see the blood cells, when they are located both within or outside the optical sectioning plane [24]. Then, the difference in the final images is determined not by interferometry and coherence but simply by the NA used. OTT underfills the collection NA, therefore it shows the entire blood flow pathway (Fig. 8). FFOCT on the contrary uses the entire NA, thus visualizes fewer vessels within the shallower depth-of-field.

In the second experiment (Fig. 9), we looked at the metabolic cell dynamics of mouse liver explant in FFOCT and OTT. Although FFOCT and OTT images were acquired from the different samples, liver samples are typically very homogeneous in terms of structures and cell densities [23], hence the comparison between both modalities should be representative. Dynamic experiments were performed with two separate FFOCT and OTT setups. Color HSV dynamic images were reconstructed from 256 sequential camera frames with the Hue, Saturation, Value channels encoding signal's central fluctuation frequency, frequency range and fluctuation amplitude, respectively [16].

Biomedical Optics EXPRESS

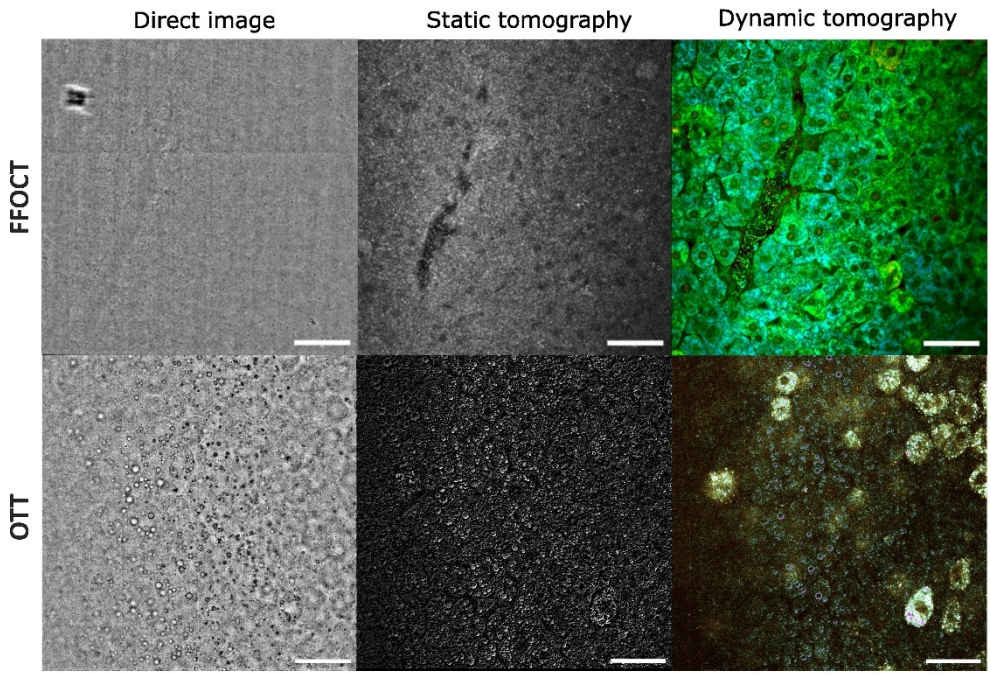

Fig. 9. Comparison of metabolic cell dynamics in mouse liver. The first sample was imaged with FFOCT in direct, static tomography, and dynamic imaging (respectively top left, center, and right panels), showing interest of dynamic FFOCT in revealing hepatocytes. The second sample was imaged with OTT in direct, static tomography and dynamic imaging (respectively bottom left, center, and right panels). In contrast to FFOCT, FFOTT detects large spherical scatterers, most likely glycogen granules found in hepatocytes. Dynamic OTT reveals some cells as well as the movements of the granules. Scale bars are 50 µm.

While the direct and static tomographic views show little contrast, dynamic imaging reveals the internal cell organelles and their metabolic activity. Direct camera frame in FFOCT captures little signal in reflectance, while transmission-based OTT shows many large particles with Gouy phase interference contrast. These particles are likely glycogen granules used to store fat in hepatocytes. Tomographic images are rather homogeneous in FFOCT with the visible nuclei, while OTT emphasizes the glycogen granules.

The dynamic FFOCT and OTT dynamic images also look significantly different. FFOCT shows a rather homogeneous signal in cell cytoplasm and lower signal in nuclei. In contrast, dynamic OTT mostly captures the movements of the glycogen granules, as we as a few hepatocytes with more intense and broadband (in terms of frequency) fluctuations. At this stage it is not clear, why only a few cells can be seen in dynamic OTT, and further investigations will be required. Nonetheless, it is not surprising that dynamic FFOCT and OTT images show different contrast since the static structures in both techniques are also seen differently.

It is important to note that in thick samples FFOCT allows to probe faster dynamic processes than OTT, because the exposure time, required to saturate the camera in reflection, can be considerably shorter (20 ms) than that in transmission (20 ms – 300 ms depending on the sample scattering/thickness).

Biomedical Optics EXPRESS

3.5. Interference artifacts in FFOCT/OTT and application to cell cultures

As was mentioned before, time-domain FFOCT produced considerable interference pattern artifacts in the zebrafish (Fig. 6(D)), obstructing the view on the fine structures. This problem is not unique to zebrafish samples and is particularly pronounced in uniform membranes and cellular mosaics, such as corneal endothelium [25]. These artifacts originate from the 2-phase tomographic image reconstruction that is known to be incapable of perfect separation of amplitude from phase [8]. In theory, it is possible to extract the clear amplitude with the 4-phase demodulation of 4 camera frames, however any small (nm) phase errors would still produce the residual interference fringes visible in the most reflective layers of the sample [24,25]. Interference fringes in FFOCT are characterized by the high contrast and long-distance correlations (across the entire millimiter FOV for uniform specular-reflecting surfaces) because the interference is biased to occur with a pre-defined single flat reference mirror plane. Moreover, the interferences exhibit a particular high spatial frequency, determined by the light source wavelength, for example, for $\lambda = 660$ nm the small 330 nm axial variation in the sample is sufficient to produce a contrasted dark-to-bright fringe (π phase shift).

OTT, being an interferometric method, also shows dark-to-bright patterns. However, their contrast is low and they exhibit only localized short-distance correlations, as they are formed by the self-interference of random scatterers. Additionally, the frequency of interferences is determined by the depth-of-field. For example, for a small scatterer with 5 μm depth-of-field the dark-to-bright modulation (π phase shift) would appear only across the 5 μm axial curvature in the sample. Thus, interference fringe frequency in OTT is an order of magnitude (10×) smaller than that in FFOCT.

The mentioned advantages of OTT are of particular importance, when imaging 2D cell cultures attached to the glass coverslip. In Fig. 10 we showed that, while FFOCT is affected by the sharp

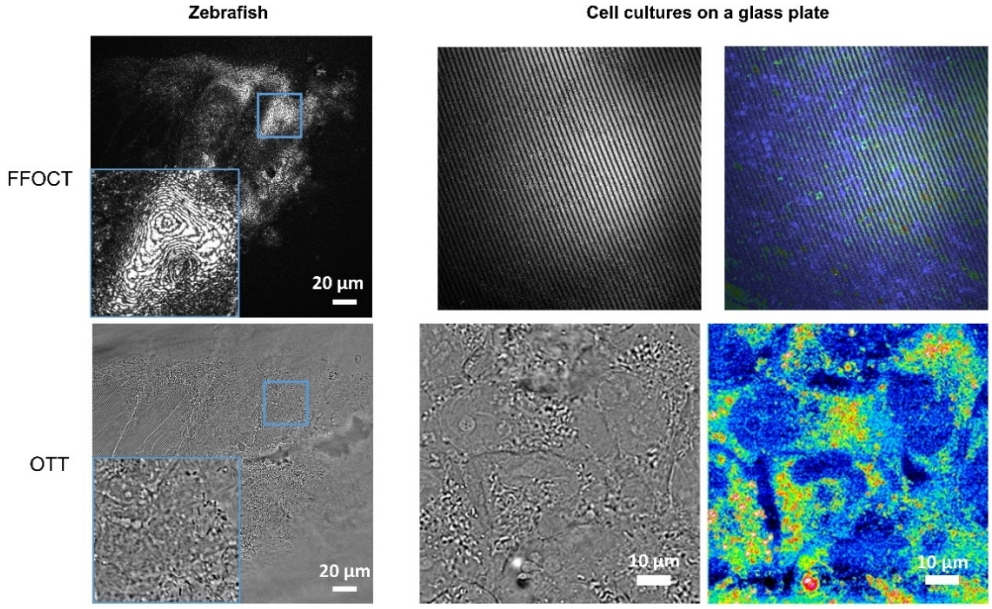

Fig. 10. OTT is less affected by the interference artefacts than FFOCT due to: (1) short-distance of interference correlations that do not have bias for a particular direction (unlike the reference mirror bias in FFOCT), (2) 10× lower fringe frequency. This opens valuable possibility of imaging 2D cell cultures on a glass slide without artefacts. The presented images of cell cultures show COS cancer cells and have different FOVs for FFOCT and OTT.

Biomedical Optics EXPRESS

interference artefacts between the coverslip and the reference mirror, OTT produces clean images. That adds OTT to the list of tomographic full-field methods capable of working with cell cultures on a slide [26–31]. The ability to perform such imaging is valuable for development of new drugs. It also opens opportunities for correlating the dynamic images obtained in 2D cultures to those obtained on similar cells in 3D environment, such as organoids, or engineered scaffolds.

4. Discussion

We conducted a comparative study of the two optical tomographic techniques, namely FFOCT and the more recent OTT using the combined experimental set-up. FFOCT provides exceptional axial resolution determined by the coherent gating of the light source. In OTT the optical sectioning is locked with the numerical aperture. However, as OTT operates in transmission, the effective numerical aperture can be tuned by varying the illumination NA. Axial Gouy phase profile follows the evolution of the effective numerical aperture and depth-of-field. Tuning illumination NA can be done simply with the aperture and scattering medium placed upon the light source. Unfortunately, the increase in resolution is accompanied by the linear decrease in contrast and effective dynamic range of the useful signal. We hypothesize this to be connected with the filling of the objective's pupil and minimization of the phase difference between the interfering transmitted and scattered light waves. The same effect is observed when imaging thick or scattering tissues as the light scattered by the tissue underneath the image plane is acting as an extended secondary source that fills the objective's pupil. Therefore, the achievable combinations of resolution and contrast depend on the sample thickness and the degree of scattering.

The above approach allowed to demonstrate 6 μm axial PSF in zebrafish larvae. However, we found that the axial PSF was not constant across the FOV but varied with the sizes of the local scatterers. The size of the scatterer influences the distribution of angular forward scattering radiation in agreement with Mie theory. For example, a small sub-micron scatterer with quasi-isotropic radiation pattern fills the detection NA and is observed within the small depth-of-field (DOF), while the scatterer of large size with radiation anisotropy underfills the NA and is seen within the larger DOF. This effect leads to imperfect optical sectioning and reduced axial resolution, as the arbitrary phase modulation step could be well adjusted (π-phase shift) for one scatterer while being imperfect for the others. This also means that by tuning the modulation step, it is possible to select the sizes of the scatterers to be emphasized in the tomographic image.

The sectioning quality is further reduced by the elongated lateral and axial wings of the PSF due to the defocus [16].

It should be mentioned that the above factors make quantitative phase imaging impractical in OTT. More precisely, in theory one can apply not only the 2-phase modulation scheme (0, π), but also the 4-phase scheme (0, $\pi/2$, π, $3\pi/2$) for decoupling of quantitative phase information from the amplitude as done in OCT [32,33]. This approach works well in OTT for isolated nanoparticles and viruses of a known size [34], as their nanometric position (phase) is directly connected to their visible brightness. On another hand, in dense biological samples the same brightness can correspond to different axial positions (phases) depending on the scatterer size that is inherently unknown. Moreover, the defocus extension of the PSF intermixes the visible phases of the neighbouring scatterers further complicating the phase recovery.

Despite the clear limitations above, OTT could resolve separate layers in volumetric zebrafish samples with high contrast and comparable quality to FFOCT. The cross-sectional and 3D views in OTT lacked the cellular details common to FFOCT but were sufficient to resolve the somites, notochord and blood vessel structures.

Comparing to the conventional transmission microscopy, OTT demonstrates improved rejection of the out-of-focus light and superior contrast. The robustness of background rejection in OTT can be attributed to the linear behavior of the axial PSF, which remains consistent between the maximum and minimum interferometric intensities, regardless of the effective NA. In other

Biomedical Optics EXPRESS

words, even when employing a phase shift designed for a higher numerical aperture, background rejection can effectively accommodate larger structures due to the linearity of the interferometric intensity. Importantly, unlike 3D deconvolution microscopy, OTT successfully operates in the dense samples, where the PSF is unknown or varies across the FOV.

OTT showed notable 10 dB SNR advantage over FFOCT caused by the 10× larger effective dynamic range due to use of the single interferometric arm, larger number of scatterers in the bigger optical sectioning volume, predominantly forward scattering of the biological tissues. Moreover, the residual interference fringe artefacts were less pronounced in OTT due to: 1) self-interference of random scatterers in OTT that does not introduce long-distance correlations biased to a certain orientation. On the contrary, FFOCT suffers from the long-distance correlations that are biased to the orientation of the flat reference mirror 2) 10× smaller interference fringe frequencies in OTT due to the extended (across the depth-of-field) 0-π Gouy phase shift. Lack of strong interference artefacts is of critical importance for imaging of fine cellular mosaic at the resolution limit and also for imaging of cell cultures on a glass slide.

Depending on the physical profile of the structure its contrast can be better in transmission-based OTT or reflection-based FFOCT. For example, thin axons of cortical neurons in murine sample were clearly seen in FFOCT while round cellular bodies were better resolved in OTT.

Both FFOCT and OTT could follow the blood flow and metabolic cell dynamics at millisecond time scale. That being said, in thick/scattering samples OTT would require long exposure times over 10 ms - 300 ms to saturate the camera and, therefore, would be able to follow only the slow dynamic processes.

Lastly, the common-path optical design of OTT is particular advantageous in terms of robustness, cost and reduced sensitivity to external vibration.

Funding. Agence Nationale de la Recherche (ANR-10-IDEX-0001-02 PSL, ANR-22-CE19-0018, ANR-22-CE45-0005).

Acknowledgements. We warmly thank Martin Carbó-Tano for preparation of zebrafish larvae and Marie Darche for providing the murine organs.

Disclosures. SA: none, OT: none, MB: none, CB: none, VM: none.

Data availability. Full resolution images generated in this paper can be obtained from the authors upon request.

References

1. J. W. Goodman, *Introduction to Fourier Optics*, 3rd ed (Roberts & Co, 2005).
2. M. Born, E. Wolf, A. B. Bhatia, P. C. Clemmow, D. Gabor, A. R. Stokes, A. M. Taylor, P. A. Wayman, and W. L. Wilcock, *Principles of Optics: Electromagnetic Theory of Propagation, Interference and Diffraction of Light*, 7th ed. (Cambridge University Press, 1999).
3. F. Zernike, "How I Discovered Phase Contrast," Science **121**(3141), 345–349 (1955).
4. Y. Park, C. Depeursinge, and G. Popescu, "Quantitative phase imaging in biomedicine," Nat. Photonics **12**(10), 578–589 (2018).
5. D. Huang, E. A. Swanson, C. P. Lin, J. S. Schuman, W. G. Stinson, W. Chang, M. R. Hee, T. Flotte, K. Gregory, C. A. Puliafito, and J. G. Fujimoto, "Optical Coherence Tomography," Science **254**(5035), 1178–1181 (1991).
6. W. Drexler and J. G. Fujimoto, eds., *Optical Coherence Tomography* (Springer International Publishing, 2015).
7. E. Beaurepaire, A. C. Boccara, M. Lebec, L. Blanchot, and H. Saint-Jalmes, "Full-field optical coherence microscopy," Opt. Lett. **23**(4), 244 (1998).
8. A. Dubois, *Handbook of Full-Field Optical Coherence Microscopy: Technology and Applications* (Pan Stanford publishing, 2016).
9. L. Quénéhervé, R. Olivier, M. J. Gora, C. Bossard, J.-F. Mosnier, E. Benoit A La Guillaume, C. Boccara, C. Brochard, M. Neunlist, and E. Coron, "Full-field optical coherence tomography: novel imaging technique for extemporaneous high-resolution analysis of mucosal architecture in human gut biopsies," Gut **70**(1), 6–8 (2021).
10. J. Scholler, K. Groux, O. Goureau, J.-A. Sahel, M. Fink, S. Reichman, C. Boccara, and K. Grieve, "Dynamic full-field optical coherence tomography: 3D live-imaging of retinal organoids," Light: Sci. Appl. **9**(1), 140 (2020).
11. E. Auksorius and A. C. Boccara, "Fingerprint imaging from the inside of a finger with full-field optical coherence tomography," Biomed. Opt. Express **6**(11), 4465 (2015).
12. V. Mazlin, P. Xiao, E. Dalimier, K. Grieve, K. Irsch, J.-A. Sahel, M. Fink, and A. C. Boccara, "In vivo high resolution human corneal imaging using full-field optical coherence tomography," Biomed. Opt. Express **9**(2), 557 (2018).

Biomedical Optics EXPRESS

13. P. Xiao, V. Mazlin, K. Grieve, J.-A. Sahel, M. Fink, and A. C. Boccara, "In vivo high-resolution human retinal imaging with wavefront-correctionless full-field OCT," Optica **5**(4), 409 (2018).
14. J. Scholler, K. Groux, K. Grieve, C. Boccara, and P. Mecê, "Adaptive-glasses time-domain FFOCT for wide-field high-resolution retinal imaging with increased SNR," Opt. Lett. **45**(21), 5901 (2020).
15. V. Mazlin, P. Xiao, J. Scholler, K. Irsch, K. Grieve, M. Fink, and A. C. Boccara, "Real-time non-contact cellular imaging and angiography of human cornea and limbus with common-path full-field/SD OCT," Nat. Commun. **11**(1), 1868 (2020).
16. V. Mazlin, O. Thouvenin, S. Alhaddad, M. Boccara, and C. Boccara, "Label free optical transmission tomography for biosystems: intracellular structures and dynamics," Biomed. Opt. Express **13**(8), 4190 (2022).
17. O. Svelto, *Principles of Lasers* (Springer US, 2010).
18. . "Mie Scattering Calculator," https://omlc.org/calc/mie_calc.html.
19. S. Johnsen and E. A. Widder, "The Physical Basis of Transparency in Biological Tissue: Ultrastructure and the Minimization of Light Scattering," J. Theor. Biol. **199**(2), 181–198 (1999).
20. O. Assayag, K. Grieve, B. Devaux, F. Harms, J. Pallud, F. Chretien, C. Boccara, and P. Varlet, "Imaging of non-tumorous and tumorous human brain tissues with full-field optical coherence tomography," NeuroImage: Clinical **2**, 549–557 (2013).
21. O. Thouvenin, C. Apelian, A. Nahas, M. Fink, and C. Boccara, "Full-Field Optical Coherence Tomography as a Diagnosis Tool: Recent Progress with Multimodal Imaging," Appl. Sci. **7**(3), 236 (2017).
22. J. Scholler, V. Mazlin, O. Thouvenin, K. Groux, P. Xiao, J.-A. Sahel, M. Fink, C. Boccara, and K. Grieve, "Probing dynamic processes in the eye at multiple spatial and temporal scales with multimodal full field OCT," Biomed. Opt. Express **10**(2), 731 (2019).
23. C. Apelian, F. Harms, O. Thouvenin, and A. C. Boccara, "Dynamic full field optical coherence tomography: subcellular metabolic contrast revealed in tissues by interferometric signals temporal analysis," Biomed. Opt. Express **7**(4), 1511 (2016).
24. V. Mazlin, P. Xiao, K. Irsch, J. Scholler, K. Groux, K. Grieve, M. Fink, and A. C. Boccara, "Optical phase modulation by natural eye movements: application to time-domain FF-OCT image retrieval," Biomed. Opt. Express **13**(2), 902 (2022).
25. V. Mazlin, K. Irsch, K. Irsch, M. Paques, J.-A. Sahel, J.-A. Sahel, J.-A. Sahel, M. Fink, and C. A. Boccara, "Curved-field optical coherence tomography: large-field imaging of human corneal cells and nerves," Optica **7**(8), 872–880 (2020).
26. T. Monfort, S. Azzollini, T. Ben Yacoub, I. Audo, S. Reichman, K. Grieve, and O. Thouvenin, "Interface self-referenced dynamic full-field optical coherence tomography," Biomed. Opt. Express **14**(7), 3491 (2023).
27. E. Auksorius and A. Claude Boccara, "Dark-field full-field optical coherence tomography," Opt. Lett. **40**(14), 3272 (2015).
28. E. M. Seromenho, A. Marmin, S. Facca, N. Bahlouli, S. Perrin, and A. Nahas, "Single-shot off-axis full-field optical coherence tomography," Appl. Phys. Lett. **121**(11), 113702 (2022).
29. R. R. Iyer, Y.-Z. Liu, C. A. Renteria, B. E. Tibble, H. Choi, M. Žurauskas, and S. A. Boppart, "Ultra-parallel label-free optophysiology of neural activity," iScience **25**(5), 104307 (2022).
30. E. Auksorius, D. Borycki, P. Stremplewski, K. Liżewski, S. Tomczewski, P. Niedźwiedziuk, B. L. Sikorski, and M. Wojtkowski, "In vivo imaging of the human cornea with high-speed and high-resolution Fourier-domain full-field optical coherence tomography," Biomed. Opt. Express **11**(5), 2849 (2020).
31. C. Pfäffle, H. Spahr, L. Kutzner, S. Burhan, F. Hilge, Y. Miura, G. Hüttmann, and D. Hillmann, "Simultaneous functional imaging of neuronal and photoreceptor layers in living human retina," Opt. Lett. **44**(23), 5671 (2019).
32. M. Žurauskas, R. R. Iyer, and S. A. Boppart, "Simultaneous 4-phase-shifted full-field optical coherence microscopy," Biomed. Opt. Express **12**(2), 981 (2021).
33. H. Iwai, C. Fang-Yen, G. Popescu, A. Wax, K. Badizadegan, R. R. Dasari, and M. S. Feld, "Quantitative phase imaging using actively stabilized phase-shifting low-coherence interferometry," Opt. Lett. **29**(20), 2399 (2004).
34. S. Alhaddad, H. Bey, O. Thouvenin, P. Boulanger, C. Boccara, I. Izeddin, and M. Boccara, *Label-Free Virus-Antibody Interaction Monitoring in Real Time by Common-Path Interferometry* (Biophysics, 2022).